Nano Energy 89 (2021) 106364

Contents lists available at ScienceDirect

Nano Energy

journal homepage: www.elsevier.com/locate/nanoen

Interfacial thermal resistance between nm-thick MoS_2 and quartz substrate: A critical revisit under phonon mode-wide thermal non-equilibrium

Hamidreza Zobeiri [a,1], Nicholas Hunter [a,1], Nathan Van Velson [b,1], Cheng Deng [c,*], Qianying Zhang [d,*], Xinwei Wang [a,*]

[a] Department of Mechanical Engineering, Iowa State University, Ames, IA 50011, United States
[b] Research and Development Department, Advanced Cooling Technologies, Inc., 1046 New Holland Ave., Lancaster, PA 17601-5688, United States
[c] School of Mechanical & Automotive Engineering, South China University of Technology, Guangzhou, Guangdong Province 510641, PR China
[d] College of Metallurgy and Material Engineering, Chongqing University of Science & Technology, University Town, Huxi Shapingba District, Chongqing 401331, PR China

ARTICLE INFO

Keywords:
Optical and acoustic phonons
Non-equilibrium thermal transport
Raman spectroscopy
Interfacial thermal resistance
TMD materials

ABSTRACT

2D materials experience a cascading energy transfer under intense laser irradiation, which leads to a strong thermal non-equilibrium between energy carriers, especially between optical (OP) and acoustic (AP) phonon branches. In previously reported Raman optothermal techniques, this non-equilibrium effect is neglected that leads to very large physics errors in interface thermal resistance characterization. Here, the optical phonon temperature rises of both in-plane and out-of-plane modes of nm-thick MoS_2 films supported on quartz substrate are determined using a steady-state Raman, and the non-equilibrium between OP-AP and their energy coupling factor are characterized by controlling the heating domain and precise calculation of Raman signal and subsequently absorbed laser power by using a transfer matrix method. It is concluded that the OP-AP temperature difference under laser heating area could be as high as ~45% of the total OP temperature rise probed by Raman. The interfacial thermal resistance (R_{tc}) between MoS_2 and quartz is reevaluated by considering this non-equilibrium effect, and it is observed that neglecting it could lead to R_{tc} over-prediction by ~100%. By determining R_{tc} using both Raman modes of MoS_2, it is observed that due to the ballistic and diffusive phonon transport and difference of interface thermal resistance among phonon modes, the flexural optical mode has a higher temperature rise than the longitudinal/transverse optical modes. This agrees well with atomistic modeling results of other 2D materials, e.g. graphene on BN.

1. Introduction

Raman spectroscopy is a proven powerful tool to characterize the thermal properties of 2D transition metal di-chalcogenides (TMD) materials, such as MoS_2 and WS_2, as well as other 2D materials. These thermal properties include thermal conductivity (k) [1–11], interfacial thermal resistance (R_{tc}) [12–15], and hot carrier diffusion coefficient (D) [16–20]. In these Raman optothermal techniques, a laser is used to excite the Raman signal as well as for heating the sample. The behavior of the Raman spectrum of that specific sample, mostly the wavenumber shift of a characteristic Raman peak, is studied, and a physical model is developed to simulate the temperature rise under the heating conditions in order to fit k, R_{tc}, or D to the model. Under laser irradiation, the hot electrons pass most of their energy to optical phonon (OP) branches, and these phonons then transfer this energy to acoustic phonon (AP) branches through several scattering mechanisms [21–23]. All Raman-based methods are based on the assumption that different phonon branches are in thermal equilibrium. In contrast, it is proved by numerical calculations that there exists a significant thermal non-equilibrium between OP and AP [22,24]. Although the heat conduction by optical branches is negligible comparing with the acoustic ones, they still affect the scattering mechanisms significantly, which indirectly leads to a reduction of thermal conduction [25,26]. This local thermal non-equilibrium between optical and acoustic phonons is ignored in the majority of the optothermal techniques.

There are very limited works about the non-equilibrium between

* Corresponding authors.
E-mail addresses: dengcheng@scut.edu.cn (C. Deng), zhangqianying526@163.com (Q. Zhang), xwang3@iastate.edu (X. Wang).
[1] H. Zobeiri, N. Hunter, and N. Van Velson contributed equally to this work.

https://doi.org/10.1016/j.nanoen.2021.106364
Received 23 April 2021; Received in revised form 6 July 2021; Accepted 19 July 2021
Available online 26 July 2021

optical and acoustic branches under laser irradiation. By calculating the cooling rate of electrons due to the temperature-dependent electron-phonon scattering mechanism that is predicted by first-principle density functional perturbation theory, it is shown that for single-layer graphene (SLG), optical phonons dominate the relaxation process of hot electrons [22]. For a suspended graphene sample under laser irradiation with a sub-micron laser spot, it is shown that the thermalization length between the flexural acoustic phonons and the other energy excitations is larger than the Gaussian beam radius of 360 nm, which shows a significant non-equilibrium between different phonon branches [24]. In another work, the hot electron relaxation processes of SLG under steady-state and transient laser irradiation were investigated using a multi-temperature model (MTM), and a separate temperature was assigned to each phonon mode. And it was found that the phonon branches are in non-equilibrium due to different cooling rates and phonon-phonon (ph-ph) and electron-phonon (*e*-ph) coupling strengths [27]. Another method to distinguish this non-equilibrium under intense local photon heating is an indirect Raman measurement based on tracking the distinct laser spot radius dependence of optical and acoustic phonon temperatures. As a result, the contribution of optical-acoustic phonon temperature rise difference to the local optical temperature rise of the suspended MoS_2 and $MoSe_2$ were determined [28]. However, that work as well as previous Raman optothermal works, lacked a precise calculation of laser power absorption and Raman signal interference as well as the fact that the input thermal, physical, and optical properties of materials could affect the calculated AP temperature rise. Understanding this thermal non-equilibrium between optical and acoustic phonons could have significant applications in a wide range of energy related topics, such as interface energy design, optimizing the cooling of electronic devices, and thermoelectric materials. For instance, it was shown that introducing super lattice precipitates and tuning the phonons' dispersion relation could modify the acoustic-optical bandgap, strengthen their scattering rate, and decrease the thermal conductivity [29,30].

In this work, the thermal non-equilibrium between OP and AP is characterized using multiple Raman optothermal measurements together with rigorous consideration of Raman signal and laser optical interference for three supported MoS_2 films on quartz. And for the first time, the interfacial thermal resistance between a nm-thick film and substrate is determined considering the inter-phonon branch non-equilibrium effects under laser heating. First, the interface resistance ($R/\!/_{tc}$) is estimated using a frequency-domain energy transport state-resolved Raman technique [31]. Then the estimated $R/\!/_{tc}$ is used in a new Raman technique to characterize the OP-AP non-equilibrium as well as refining the estimated $R/\!/_{tc}$ with minimum dependency on optical and thermal properties of materials on AP temperature rise calculation. Finally, the OP-AP energy coupling factor is determined using precise calculation of Raman intensity-weighted average temperature rise and laser absorption of MoS_2 film by using a transfer matrix method (TTM), which considers all backward and forward scatterings inside the thin film and substrate.

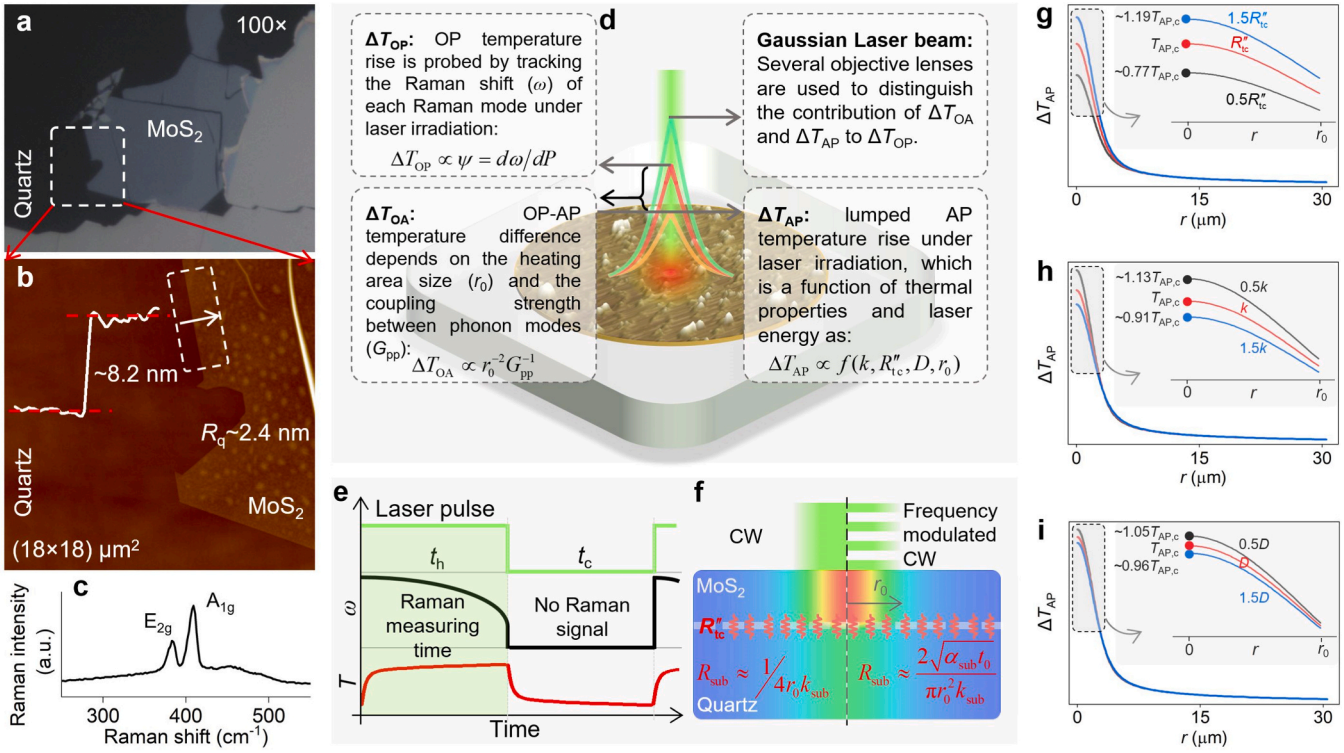

Fig. 1. (a) Optical image of Sample #1, which shows the MoS_2 nano-sheet supported on a quartz substrate. (b) AFM image of this sample to find its thickness and roughness profiles. The image corresponds to the white dashed rectangle in figure (a). The thickness profile is related to the dashed rectangle, as shown in this AFM image. (c) Raman spectrum of MoS_2 and its two main Raman modes that are used in this work to distinguish the acoustic and optical phonon temperature rises. (d) Schematic of supported MoS_2 on quartz and physics of thermal non-equilibrium between OP and AP under laser irradiation. This figure shows the cascading energy transfer between two phonon modes within the heating area. Outside this area, OP and AP are in thermal equilibrium. (e) During each laser pulse heating of FET-Raman (t_h), the Raman wavenumber (ω) red shifts due to the temperature rise (red curve). (f) The physics of FET-Raman and the fact that the contribution of $R/\!/_{tc}$ to the total thermal resistance between MoS_2 and substrate is different, and it makes it possible to determine $R/\!/_{tc}$ using FET-Raman. This is because R_{sub} is different under the steady and transient states. (g-i) The calculated local lumped AP temperature rise distribution (T_{AP}) of MoS_2 film in the radial direction under 4 μm diameter laser spot. In each plot, one of these parameters, $R/\!/_{tc}$, or k, or D, is changed by ± 50%. It is shown than T_{AP} is more sensitive to $R/\!/_{tc}$ than the other two parameters, and least sensitive to D. The inset of each plot shows the zoom-in view of the dashed rectangle to show the differences between three cases in the laser spot region. $T_{AP,c}$ is the local AP temperature rise of MoS_2 at the center of laser spot calculated using the default parameter k, D, or $R/\!/_{tc}$.

2. Results

2.1. Preparation and characterization of supported MoS_2

Here, three nm-thick supported MoS_2 samples are prepared to distinguish the optical and acoustic phonon temperature rises and measure the interface resistance between the MoS_2 film and quartz substrate. The samples are prepared using a modified scotch tape-assisted mechanical exfoliation technique (see "Methods Section"), which guarantees high quality and pristine structure. Fig. 1(a) shows the optical image of Sample #1 prepared using this method. Also, atomic force microscopy (AFM) measurement is conducted for each sample to find its thickness profile and root mean square roughness (R_q), as shown in Fig. 1(b). Fig. S1 presents the optical and AFM images of the other two supported MoS_2 films. Based on this characterization, the thicknesses (t) of these three films are 8.2, 12.6, and 15.3 nm, respectively (Sample #1 to #3). Also, R_q values are 2.4, 1.4, and 1.9 nm, respectively. The relative roughness of these films, which is defined as (R_q/t), is maximum for Sample #1 (~0.3), which is evident from the AFM images. Note that Sample #1 is used in all of the following sections to illustrate the details of our analysis, and the results of the other two samples are summarized in related tables and figures. Fig. 1(c) shows the typical Raman spectrum of MoS_2 and its two Raman modes, namely $E_{2\,g}$ and $A_{1\,g}$ (see "Methods Section" for more about the Raman system). These two modes are used to study the non-equilibrium between OP and AP. The $E_{2\,g}$ mode is doubly degenerate and is related to the in-plane vibrations of two S atoms in the opposite direction with respect to Mo in the x-y plane, and $A_{1\,g}$ is nondegenerate and corresponds to the out-of-plane vibrations of S atoms [32,33].

2.2. Physics of optical-acoustic phonon coupling under laser excitation

2.2.1. OP-AP thermal non-equilibrium and effects of physical parameters: a general picture

Under laser irradiation, the electrons in the valence band of MoS_2 are excited to the conduction band. These excited electrons cool down within a very short period of time and transfer most of their energy to the optical phonon branches (OP) without significant direct contribution to thermal transport inside the supported MoS_2 [16]. This process takes place within a short time, in order of ns or shorter. Therefore, it can be assumed that the energy of absorbed photons is transferred to the OP instead of being diffused by hot electrons. This effect is shown by density functional theory (DFT) calculations by Ruan's group [22]. Based on these calculations, the electron-phonon coupling factor as a function of the phonon's wave vector was calculated. It was shown that the coupling factor between hot electrons and optical phonons is more significant and larger than the one between electrons and acoustic phonons by a factor of ~15. Therefore, the energy transferred from hot electrons to acoustic phonons is minimal compared with that to optical branches. Upon receiving energy from hot electrons, OP couple with AP through various anharmonic coupling processes [34,35]. This coupling process between OP and AP can vary depending on the OP branch (longitudinal: LO, transverse: TO, flexural: ZO). Then, the AP transfers the energy through the entire sample by heat conduction. Note that the thermal conductivity of OP is much smaller than that of AP [26,36,37]; therefore, they contribute very little to heat conduction. However, their coupling strength with AP affects the heat conduction significantly. Under the laser spot, the local temperature difference between electrons and OP (ΔT_{eO}) is proportional to the local absorbed power (I). This is due to the negligible effect of hot carrier diffusion on energy transport. Also, since the heat conduction by OP is minimal, it can be assumed that the temperature difference between each OP and AP branch (ΔT_{OA}) is proportional to I, and for constant laser energy, it is proportional to the inverse of laser spot area (r_0^{-2}). Here, r_0 is the laser spot radius.

The local AP temperature rise depends on the laser spot size and other parameters that affect thermal conduction, such as thermal conductivity (k), interfacial thermal resistance ($R/\!/_{tc}$), and hot carrier diffusion (D) [$\Delta T_{AP} \propto f(R/\!/_{tc},\ k,\ D,\ I)$]. These three parameters have different contributions to ΔT_{AP}, which will be shown later. Note that here ΔT_{AP} is a lumped average AP temperature rise rather than each AP branch individual temperature rise. Therefore, in the laser irradiation area, the relationship between these temperature rises could be written as: $\Delta T_{OP} = \Delta T_{AP} + \Delta T_{OA} = \Delta T_{AP} + C/r_0^2$. Here, C is the proportionality constant related to ΔT_{OA} and depends on several parameters, such as the total absorbed laser energy and the energy coupling factor between OP and AP (G). Note that outside the heating area, there is no temperature difference between OP and AP. This theory is proved in detail in previous work by Wang et al. for TMD materials and graphene [28]. This physical process is shown in Fig. 1(d) that illustrates the cascading energy transfer from OP to AP within the laser heating area.

Here, ΔT_{OP} is characterized by measuring the laser power dependence of the Raman shift ($d\omega/dP$) of $E_{2\,g}$ and $A_{1\,g}$ modes, separately. $d\omega/dP$ is actually proportional to Raman intensity-weighted temperature rise (in space and time domains), and not just simply the local temperature rise of the MoS_2 film. This is considered in our numerical calculation in detail, which is discussed in the following sections. As mentioned in the previous paragraph, ΔT_{AP} depends on several thermal properties. Fig. 1(g-i) shows the dependency of ΔT_{AP} of the MoS_2 film on $R/\!/_{tc}$, k, and D. For each case, ΔT_{AP} is calculated for three different values of that property with 50% uncertainty assumption, and it is shown that ΔT_{AP} is more sensitive to $R/\!/_{tc}$, and then k, and D is the least sensitive parameter. To perform this analysis, the default values of $R/\!/_{tc}$, k, and D are taken as 2×10^{-6} m^2KW^{-1}, 30 Wm^{-1} K^{-1}, and 4 cm^2 s^{-1}, respectively, and the laser spot radius is 1.8 μm (see "Methods Section" for more details about our physical models and numerical calculation) [2,4,5,17,38]. In all of the previous works based on optothermal Raman spectroscopy, this non-equilibrium between OP and AP was not considered in measuring $R/\!/_{tc}$ or other thermal properties, and it was assumed that ΔT_{OP} and ΔT_{AP} are equal in the laser heating region. Here, for the first time, $R/\!/_{tc}$ is determined by considering the cascading energy transfer between phonon modes, and finally the OP-AP energy coupling factor is determined.

2.2.2. Interface thermal resistance without considering OP-AP thermal non-equilibrium

As it was shown in the previous part, interfacial thermal transport at the MoS_2-quartz interface is one of the main parameters controlling ΔT_{AP}. Here, $R/\!/_{tc}$ is estimated first based on the frequency-domain energy transport state-resolved Raman (FET-Raman). In this technique, two different energy transport states are constructed as (1) steady-state and (2) transient state, using a CW and an amplitude-modulated CW laser. Under each heating state, laser irradiates the MoS_2 film, and the Raman shift (ω) of both modes are measured under different laser powers (P). Based on this experiment, the Raman shift power coefficient (RSC) of each heating mode is found as: $\psi = d\omega/dP$. ψ of each Raman peak is proportional to the Raman intensity-weighted OP temperature rise under each state and depends on several factors, such as Raman temperature coefficient ($d\omega/dT$), laser absorption coefficient (α), k, D, and $R/\!/_{tc}$. Using the ψ values under these two modes (ψ_{CW20} and ψ_{F20}) with same objective lens (20 ×), a normalized RSC is found as: $\Theta_{F20} = \psi_{F20}/\psi_{CW20}$. Now, Θ_{F20} is a function of only thermal properties, and there is no effect of $d\omega/dT$ and α on it. Also, the lumped Raman intensity-weighted acoustic temperature rise of MoS_2 under both states (ΔT_{CW20} and ΔT_{F20}) are calculated numerically with our 3D modeling for various $R/\!/_{tc}$, k, and D values. A new parameter is defined as the theoretical normalized AP temperature rise as: $\Theta_{F20,th} = \Delta T_{F20}/\Delta T_{CW20}$ (see "Methods Section" for more details about the FET-Raman physics).

For a wide range of k and D values, $\Theta_{20\,F,th}$ is calculated and normalized by the $\Theta_{20\,F,th}$ calculated using the default k and D ($\Theta^*_{F20,th} = \Theta_{F20,th}/\Theta_{F20,th,default}$) mentioned in the last section. Fig. 2(c) shows the

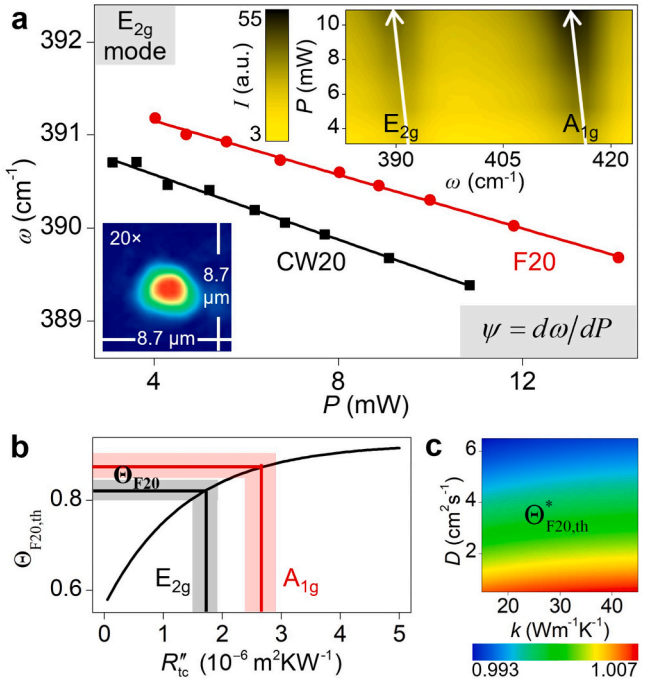

Fig. 2. (a) The measured ψ using the $E_{2\,g}$ mode of MoS_2 under both heating states to find Θ_{F20}. It shows that the slope of the F20 data is lower than CW20 due to the lower temperature rise under the amplitude-modulated laser. The top right inset shows the 2D contour of Raman intensity as a function of laser power and peak position under CW20 heating state. The two arrows show the redshift of both Raman modes with increased laser power. The bottom left inset shows the laser spot under 20 × objective lens. This contour is analyzed by a Gaussian fitting method to find the laser spot radius (r_0 at e^{-1}) that is used in our numerical simulation. (b) Measured R''_{tc} of Sample #1 using both Raman modes. The black curve shows the calculated $\Theta_{F20,th}$ for varied R''_{tc} values. Shaded areas represent the uncertainty of the determined R''_{tc} due to the uncertainty of Θ_{F20} values. (c) Calculated $\Theta^*_{F20,th}$ for a fixed R''_{tc} (2×10^{-6} m^2 KW^{-1}) as a function of k and D. This contour shows that FET-Raman using 20 × objective significantly suppresses the effects of the input values of k and D on the calculated $\Theta_{F20,th}$. This effect is less than 1% when k or D are changed by 50%.

$\Theta^*_{F20,th}$ contour for a constant R''_{tc} (2×10^{-6} m^2KW^{-1}) under various k and D values. This contour shows that $\Theta^*_{F20,th}$ is almost independent of k and D. Therefore, $\Theta_{20\,F,th}$ is independent of input values of k and D. However, the contribution of R''_{tc} on ΔT_{CW20} and ΔT_{F20} is different. The total thermal resistance between MoS_2 thin film and substrate (R_T) is the sum of the interfacial thermal resistance ($=R''_{tc}/\pi r_0^2$) and substrate's thermal resistance (R_{sub}). Although the interfacial thermal resistance is the same under both states, R_{sub} is different, which leads to different contributions of R''_{tc} to R_T and subsequently ΔT_{CW20} and ΔT_{F20} (see "Methods section" for more about this analysis). Therefore, $\Theta_{F20,th}$ is a function of R''_{tc}. Fig. 2(b) shows $\Theta_{F20,th}$ for a range of R''_{tc} using constant default k and D values (black solid curve). The experimental and calculation parts of FET-Raman results are produced by using a 500 kHz modulation frequency (f) of the amplitude-modulated laser. The accuracy of the FET-Raman technique depends on f, and a detailed numerical analysis is conducted to find the most suitable f for this experiment (see "Methods section"). Fig. 2(a) presents the results of the Raman experiment to measure ψ_{CW20} and ψ_{F20} for Sample #1 for both Raman modes. Based on these two RSC values, Θ_{F20} is found as 0.83 ± 0.01 and 0.88 ± 0.02 for $E_{2\,g}$ and $A_{1\,g}$ modes, respectively. The right inset of this figure shows the 2D contour of Raman intensity of both Raman modes under CW20 heating state, and the two white arrows indicate the redshift of each Raman peak with increased laser power. R''_{tc} for each of the $A_{1\,g}$ and $E_{2\,g}$ modes is determined by equating Θ_{F20} with $\Theta_{F20,th}$, as shown in Fig. 2(b). The bottom left inset of Fig. 2(a) shows the intensity contour of the laser spot under 20 × objective lens and is used to find r_0. A similar plot is shown for the $A_{1\,g}$ mode in the Supporting Information (Fig. S3). Based on this analysis, R''_{tc} of Sample #1 is determined as (1.79 ± 0.15)× 10^{-6} m^2 KW^{-1} and (2.69 ± 0.47)× 10^{-6} m^2KW^{-1} for $E_{2\,g}$ and $A_{1\,g}$ Raman modes, respectively.

Table 1 includes the result of this first estimation for all of the three MoS_2 films. Note that this measurement is based on the assumption that under laser irradiation, all phonon branches are in thermal equilibrium ($\Delta T_{OA} = 0$). However, as mentioned in previous sections, this argument is an approximation, and there is a thermal non-equilibrium between OP and AP. As will be shown in the next sections, this non-equilibrium gets weaker when the laser heating area is larger, and its effect is less than 10% under 20 × objective (r_0~2 μm). Therefore, FET-Raman could be used to do a first-estimation of R''_{tc}, and in the next section, this value is refined by considering the non-equilibrium between OP and AP branches. Note that real laser spot radii are used to perform the calculation in this section and next ones. The measured values of r_0 are reported in Table S1. The slight differences between laser spot size of CW laser ($r_{0,CW20}$) and amplitude-modulated CW laser ($r_{0,F20}$) under 20 × is due to the slight difference of focus levels.

This table shows the measured R''_{tc} for all three samples are in close range, and the differences between them could be mostly related to the sample's structure and the MoS_2-quartz interface bonding quality. As shown in Table 1, the measured Θ_{F20} and subsequently the determined R''_{tc} using the $A_{1\,g}$ mode is generally higher than R''_{tc} using the $E_{2\,g}$ peak. The $E_{2\,g}$ mode is related to the in-plane vibrations, or LO and TO phonon modes, and $A_{1\,g}$ peak corresponds to the out-of-plane vibrations or ZO phonon mode. Each of these phonon modes has its own specific energy coupling factor with the acoustic branches, and usually, the temperature rise of the in-plane modes is larger than the ZO modes [27]. This leads to lower Θ_{F20} for $E_{2\,g}$ mode and, as a result, smaller R''_{tc} value. The energy coupling factors are determined in the next sections and prove this argument. The uncertainty of this measurement using the FET-Raman technique could be reduced by optimizing the frequency that is used to conduct the transient heating state. It is shown in our previous works that the accuracy of FET-Raman reaches maximum when the normalized Raman shift power coefficient is ~0.75. Also, another option could be using a nanosecond (ns) pulsed laser instead of a frequency-modulated CW laser to generate the transient state. In that case, since the heat diffusion length under the ns state is much shorter than the CW state and the heating is more localized, there will be more effects of R''_{tc} on the temperature rise of thin-film compared with the CW state. This effect is well studied in our previous works. Note here we use the frequency-modulated laser since it simplifies the experiment [12,14].

2.3. *Optical-acoustic phonon temperature difference and rigorously determined R''_{tc}*

The estimation of R''_{tc} using FET-Raman was based on the assumption that $\Delta T_{OP} = \Delta T_{AP}$ under 20 × lens, while it was mentioned in Section 2.2 that $\Delta T_{OP} = \Delta T_{AP} + \Delta T_{OA}$. To consider the effects of ΔT_{OA} on thermal transport and characterize them, three laser heating modes are generated using a CW laser. These modes are CW20, CW50, and CW100, which correspond to CW laser heating with 20 ×, 50 ×, and 100 × objective lenses, respectively. ΔT_{AP} under these states is controlled by k, D, and R''_{tc}. Fig. 3(a) shows the calculated T_{AP} contour of MoS_2 film and substrate under these three states for varied values of k, D, and R''_{tc}. Each of these three parameters (k, D, and R''_{tc}) has a different contribution to ΔT_{AP} under each heating mode (ΔT_{CW20}, ΔT_{CW50}, and ΔT_{CW100}). Effects of k and D are more significant under smaller laser spot sizes, while R''_{tc}'s effects are more significant for larger r_0 values. The hot carrier diffusion and in-plane heat diffusion effects are more important when r_0 is small or comparable to the diffusion lengths, and in an extreme case that r_0 is larger than the sample radius, the temperature rise of the sample is controlled mainly by R''_{tc} [5]. Therefore, CW50 heating mode is the moderate case between CW20 and CW100. Also, the

Table 1
Results of the FET-Raman experiment and the first-estimation of $R/\!/_{tc}$ using both $E_{2\,g}$ and $A_{1\,g}$ Raman modes.

Sample #	Thickness (nm)	Raman mode	ψ_{CW20} ($cm^{-1}mW^{-1}$)	ψ_{F20} ($cm^{-1}mW^{-1}$)	Θ_{F20}	$R/\!/_{tc}$ (10^{-6} m^2KW^{-1})
1	8.2	$E_{2\,g}$	-0.175 ± 0.002	-0.145 ± 0.001	0.83 ± 0.01	1.79 ± 0.15
		$A_{1\,g}$	-0.163 ± 0.002	-0.143 ± 0.002	0.88 ± 0.02	2.69 ± 0.47
2	12.6	$E_{2\,g}$	-0.219 ± 0.005	-0.172 ± 0.002	0.78 ± 0.02	4.26 ± 1.21
		$A_{1\,g}$	-0.178 ± 0.004	-0.141 ± 0.003	0.79 ± 0.02	5.46 ± 1.85
3	15.3	$E_{2\,g}$	-0.263 ± 0.004	-0.185 ± 0.001	0.70 ± 0.01	3.70 ± 0.87
		$A_{1\,g}$	-0.249 ± 0.003	-0.176 ± 0.001	0.71 ± 0.01	4.57 ± 1.22

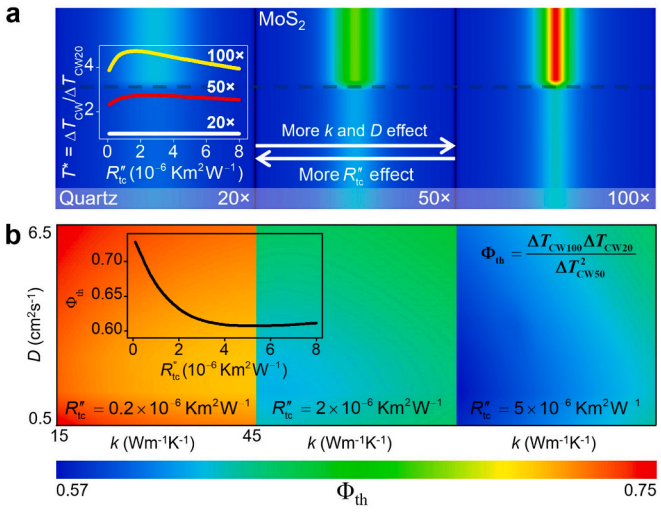

Fig. 3. (a) Lumped AP temperature contour of MoS_2 and quartz under three steady-state heating. These three states are constructed to distinguish the thermal non-equilibrium between OP and AP independent of k, D, and $R/\!/_{tc}$ values. The horizontal and vertical size of each panel is 15 μm and 20 nm, respectively. The inset of this figure shows the moderate effect of $R/\!/_{tc}$ on T^* under 50 × objective. The black dashed line indicates the MoS_2-quartz interface. (b) Calculated Φ_{th} for three different $R/\!/_{tc}$ values and wide ranges of k and D. These contours show that Φ_{th} is independent of k, D, and $R/\!/_{tc}$ (for values larger than ~1 ×10^{-6} Km^2 W^{-1}). The horizontal axis (k) of three panels share the same range of k: 15–45 Wm^{-1} K^{-1}. The inset of this figure shows the Φ_{th}-$R/\!/_{tc}$ plot for a constant k and D.

term "2D materials" is referred to the few-layered materials. For larger thicknesses (in order of tens of nm), the hot carrier diffusion and heat conduction in the film, especially in the thickness direction, become more significant and should be well considered in the thermal analysis.

For a constant k and D, the normalized ΔT_{AP} (T^*) under each state with ΔT_{CW20} ($T^* = \Delta T_{CW}/\Delta T_{CW20}$), and as a function of $R/\!/_{tc}$ of Sample #1 is shown in the inset of Fig. 3(a) to show that $R/\!/_{tc}$'s effect on CW50 is moderate compared with two other cases. Laser spot radii under these three heating states for all three samples are indicated in Table S1. A similar study is conducted for k and D effects, as shown in Fig. S4. Based on this analysis, a new parameter is defined (Φ_{th}) as: $\Phi_{th} = (\Delta T_{CW100}\Delta T_{CW20})/(\Delta T^2_{CW50})$. Fig. 3(b) shows the calculated Φ_{th} contour for a wide range of k, D, and $R/\!/_{tc}$, and shows that k and D have negligible effects on Φ_{th} (less than 4%). Regarding the effects of $R/\!/_{tc}$ on Φ_{th}, if $R/\!/_{tc}$ is more than 1 × 10^{-6} Km^2W^{-1}, it is minimal (less than 6%). However, for smaller $R/\!/_{tc}$ values, especially in the order of 10^{-7} Km^2 W^{-1}, the Φ_{th} change can be up to 20%. The inset of this figure shows Φ_{th}-$R/\!/_{tc}$ plot for this sample with the default D and k values. This analysis shows that for $R/\!/_{tc}$ larger than 1 × 10^{-6} Km^2 W^{-1}, which is the range of our analysis in this work, Φ_{th} could be considered as a constant value with less than 6% uncertainty. The estimated $R/\!/_{tc}$ using FET-Raman (Table 1) are all more than 1 × 10^{-6} Km^2 W^{-1}; therefore, $R/\!/_{tc}$'s effect on Φ_{th} is also minimal. This is due to the fact that ΔT_{CW50} in the denominator compensates for the differences between the effects of k, D, and $R/\!/_{tc}$ on ΔT_{CW20} and ΔT_{CW100} as extreme cases. Similar Φ_{th}-$R/\!/_{tc}$ plots for the other two samples are shown in Fig. S5.

The experimental counterpart of Φ_{th} could be written as: $\Phi_{exp} = [(\Delta T_{OP100} - \Delta T_{OA100})(\Delta T_{OP20} - \Delta T_{OA20})]/[(\Delta T_{OP50} - \Delta T_{OA50})^2]$. This is due to the fact that under each heating state we have $\Delta T_{AP} = \Delta T_{OP} - \Delta T_{OA}$. Also, as mentioned earlier: $\Delta T_{OP} \propto \psi$, and $\Delta T_{OA} = C/r_0^2$. Therefore, Φ_{exp} could be rewritten as: $\Phi_{exp} = [(\Delta T^*_{OP100} - C/r^2_{0,100})(\Delta T^*_{OP20} - C/r^2_{0,20})]/[(\Delta T^*_{OP50} - C/r^2_{0,50})^2]$. Here, ΔT^*_{OP} is defined as the normalized RSC values with ψ under 20 × objective lens as: $\Delta T^*_{OP} = \psi/\psi_{20}$. Fig. 4(a) shows the results of this experiment for the first sample using the $E_{2\,g}$ mode. The data points are fitted linearly to find ψ. The slope of these three lines shows moderate heating under CW50 state again. Similar results for the $A_{1\,g}$ mode are shown in Fig. S6. All of the measured ΔT^*_{OP} are shown in Fig. 4(b). The decreasing trend of these plots versus thickness is due to the below physics. With the same absorbed laser power, the temperature rise will become higher with reduced laser spot because the substrate thermal resistance is proportional to r_0^{-1} and the interface thermal resistance is proportional to r_0^{-2}. However, when the laser spot is smaller, the in-plane heat conduction and hot carrier diffusion effect becomes stronger, which will reduce the temperature rise. Such reduction is stronger for thicker films because of this larger in-plane cross-sectional area.

With known ψ values under three states and constant Φ_{th} value, we are able to estimate the factor C, and finally, the contribution of ΔT_{OA} to the total OP temperature rise under each laser heating state, which represents the non-equilibrium between OP and AP as $C/\Delta T^*_{OP} r_0^2$. The constant value of Φ_{th} is calculated using the estimated $R/\!/_{tc}$ from FET-Raman. Several Raman experiments are conducted to find ψ under three objective lenses for all three samples and both Raman modes, and the results are included in Table 2.

Now, Θ_{F20} from Section 2.3 is refined by considering OP-AP non-equilibrium effects as: $\Theta_{F20} = \psi_{AP,F20}/\psi_{AP,CW20} = (\Delta T^*_{OP,F20} - C/r^2_{0,F20})/(\Delta T^*_{OP,20} - C/r^2_{0,20})$, and the updated value of $R/\!/_{tc}$ is determined from FET-Raman calculation. Several iterations are conducted, as shown in the inset of Fig. 4(c), until $R/\!/_{tc}$ and C are converged with less than 1% difference. The converged values of $R/\!/_{tc}$ for all samples are reported in Table 2. Also, the contribution of ΔT_{OA} to the total ΔT_{OP} ($[C/\Delta T^*_{OP} r_0^2] \times 100$) under several laser objectives and for all samples is shown in Fig. 4(c). This plot indicates that for all three samples, the non-equilibrium between OP and AP becomes more significant for smaller laser heating areas, and this is consistent with our previous discussion in Section 2.2.

2.4. Precise determination of OP-AP energy coupling factor (G)

All of the above discussion is based on 1 mW irradiating laser on MoS_2 top surface (for both ψ and ΔT_{CW} values), and OP and AP temperatures are Raman intensity-weighted average. As mentioned earlier and in the Methods section, the numerical modeling calculates the lumped AP temperature rise, and the OP temperature rise is determined using the ratio of ψ values and these calculation results. ΔT_{OA} ($= C/r_0^2$) determined in the previous section reflects the contribution under 1 mW irradiating laser power and is also a Raman intensity-weighted average (see "Methods section"). To determine the energy coupling factor

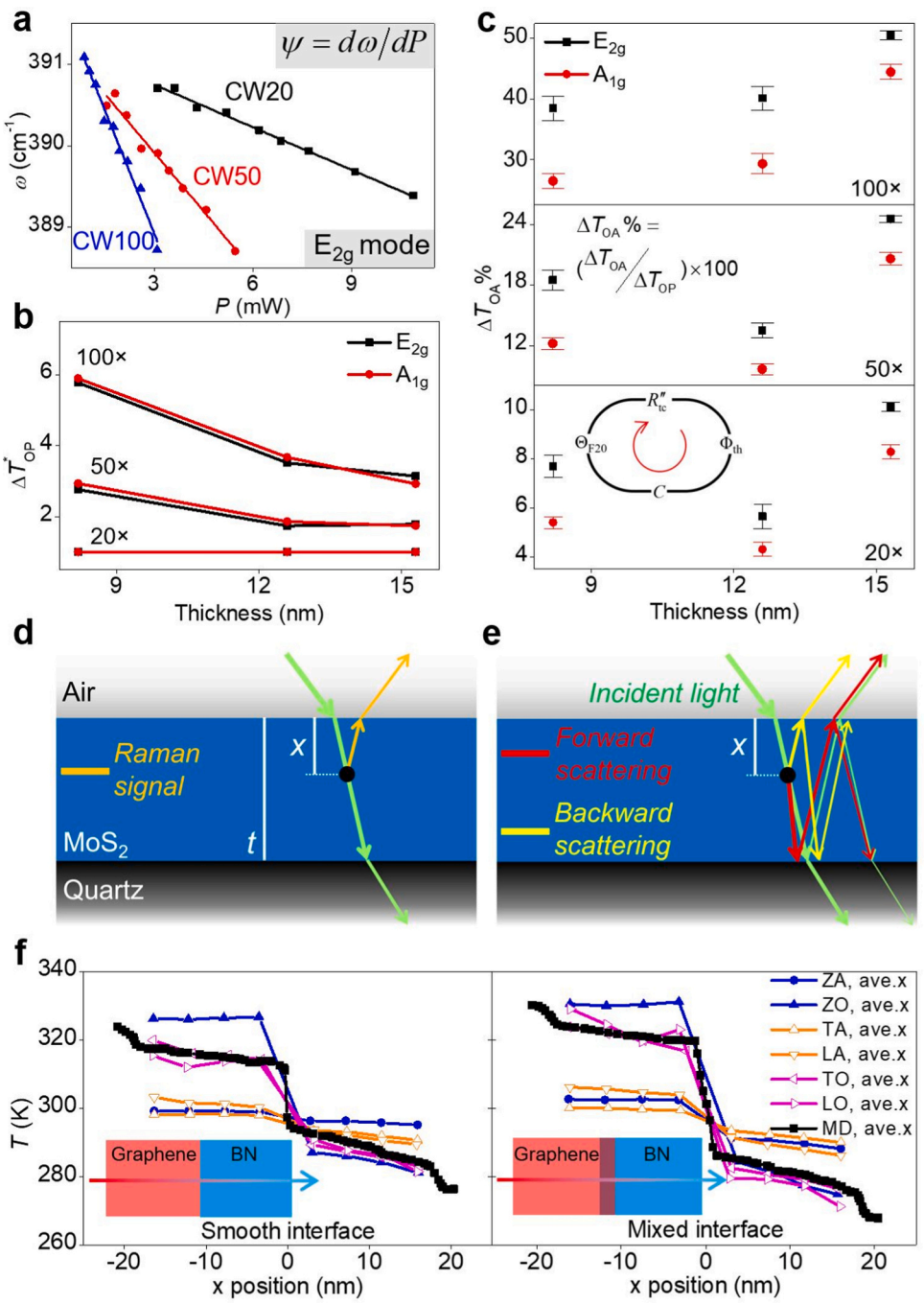

Fig. 4. (a) ψ values under CW20, CW50, and CW100 heating states using the E_{2g} mode. The experimental data points are fitted linearly to determine ψ under each heating state. This plot also shows the moderate heating under 50 × objective lens. (b) Normalized ψ values (ΔT^*_{OP}) for all samples and both modes. The decreasing trend of ΔT^*_{OP} with MoS_2 thickness is due to the higher temperature rise of thinner films under the same laser heating power for smaller laser spots. (c) Contribution of thermal non-equilibrium between OP-AP for three samples measured by using two MoS_2 Raman modes. Inset of bottom panel shows the schematic of the iteration cycle to determine the precise R''_{tc} and C values by coupling FET-Raman and OP-AP thermal non-equilibrium measurement. The convergence threshold is less than 1%, and it takes 3–4 iterations for this cycle to converge with this limit. (d) and (e) show the physics of Raman signal intensity calculation using classical (I_a) and rigorous multi-reflection (I_b) methods, respectively. (f) The temperature of different modes of phonons across two different graphene-BN interfaces (smooth and mixed) [39]. Here, T_{MD} is the lumped phonon temperature that is calculated using molecular dynamics modeling.

Table 2
Converged R''_{tc} and determined G factor for three supported MoS_2 films and both Raman modes.

Sample #	Raman mode	ψ_{CW50} (cm^{-1}mW^{-1})	ψ_{CW100} (cm^{-1}mW^{-1})	R''_{tc} (10^{-6} m^{2}KW^{-1})	G (10^{15} Wm^{-3}K^{-1})
1	E_{2g}	-0.481 ± 0.009	-1.010 ± 0.015	1.35 ± 0.17	3.05 ± 0.17
	A_{1g}	-0.477 ± 0.007	-0.959 ± 0.016	2.24 ± 0.54	2.17 ± 0.09
2	E_{2g}	-0.381 ± 0.008	-0.772 ± 0.020	2.84 ± 0.95	5.49 ± 0.35
	A_{1g}	-0.331 ± 0.007	-0.654 ± 0.017	3.50 ± 1.12	3.60 ± 0.23
3	E_{2g}	-0.470 ± 0.005	-0.828 ± 0.006	2.33 ± 0.61	3.37 ± 0.11
	A_{1g}	-0.434 ± 0.006	-0.728 ± 0.009	3.73 ± 0.95	2.06 ± 0.08

between OP and AP, the precise absorbed power (I_b) is needed, which depends on multiple reflections of both the incident light and the Raman scattered light off of thin-film interfaces, taking into account the backward and forward generated Raman signal. Here, I_b for 1 mW laser irradiation under several objective lenses with experimental r_0 values is calculated, and based on this a new OP-AP temperature difference ($\Delta T_{OA,b}$) is calculated using a transfer matrix method (TMM).

The Raman signal generated at each location in the radial and

thickness directions (r, z) of MoS_2 thin film under a Gaussian laser beam is proportional to the local optical field intensity (I_{opt}) of the incident light, which could be written as: $I_{opt}(r,z) = 0.5c\varepsilon_0 n|E(z)|^2\exp(-r^2/r_0^2)$. Here, c, ε_0, and n are speed of light, the permittivity of free space, and the refractive index of MoS_2, respectively. $E(z)$ is the electric field amplitude at each location in the thickness direction and can be readily calculated using TMM. The generated Raman signal at each location propagates in both backward and forward directions. The backward and forward Raman scattering emitted at the surface of MoS_2 film are $E_{0,b}$ and $E_{0,f}$. $E(z)$, $E_{0,b}$, and $E_{0,f}$ are calculated from a thin film system based on TMM, and the total Raman signal generation from MoS_2 supported on quartz under Gaussian laser beam for incoherent (not in phase) backward and forward Raman scattering could be written as:

$$I_{Raman} = \int_t |E(z)|^2\left(|E_{0,b}|^2 + |E_{0,f}|^2\right)\exp\left(-r^2\Big/r_0^2\right)2\pi r dr dz. \quad (1)$$

More about this TMM calculation could be found in our previous work by Van Velson et al. [40]. I_{Raman} is the intensity of the Raman signal of each Raman active mode measured by the Raman system. Also, the local OP-AP temperature difference [$\Delta T_{\mathrm{OA}}(r, z)$] is proportional to absorbed laser power at each location and the coupling factor (G), as:

$$\Delta T_{\mathrm{OA}}\left(r,z\right) = \frac{\delta}{\tau_{\mathrm{L}}G}\cdot 0.5c\varepsilon_0 n\cdot|E(z)|^2\exp\left(-r^2\Big/r_0^2\right) \quad (2)$$

δ is the fraction of laser energy transferred from the measured Raman mode OP to AP ($0 < \delta < 1$). Here, we assume that energy is transferred uniformly to optical phonons. Therefore, δ takes 2/3 for $E_{2\,g}$ mode (LO and TO) and 1/3 for $A_{1\,g}$ mode (ZO). Therefore, the Raman intensity-weighted average OP-AP temperature difference ($\Delta T_{\mathrm{OA,b}}$) is found as:

$$\Delta T_{\mathrm{OA,b}} = \frac{\int \Delta T_{\mathrm{oa}}(r,z)dI_{Raman}}{\int dI_{Raman}} = 0.25\times\frac{\delta c\varepsilon_0 n}{\tau_{\mathrm{L}}G}\cdot\frac{\int|E(z)|^4\left(|E_{0,b}|^2+|E_{0,f}|^2\right)dz}{\int|E(z)|^2\left(|E_{0,b}|^2+|E_{0,f}|^2\right)dz}. \quad (3)$$

Additionally, the total absorbed laser power by MoS_2 film (I_{b}) is found as:

$$I_{\mathrm{b}} = \pi r_0^2\cdot\frac{cn\varepsilon_0}{2}\cdot\int_0^t\frac{|E(z)|^2}{\tau_{\mathrm{L}}}dz. \quad (4)$$

$\Delta T_{\mathrm{OA,b}}$ of each mode is a function of OP-AP coupling factor (G). Finally, the energy coupling factor between OP-AP is determined by equating $\Delta T_{\mathrm{OA,b}}/I_{\mathrm{b}}$ with $\Delta T_{\mathrm{OA}}/I_{\mathrm{a}}$. The physics of calculating I_{b} is presented in Fig. 4(e). Compared with the classical calculation of Raman intensity (I_{a}), that is shown in Fig. 4(d), the backward and forward Raman scatterings at each location (x) and their multi-reflection inside the MoS_2 film are considered to find the precise absorbed laser power. Additionally, our optical interference model considers the discontinuity of Raman signal within the film due to local Raman signal generation. Table 2 summarizes the G of two Raman modes for three samples. It can be seen from this table that the measured G values for the three samples are in the same range and is larger for $E_{2\,g}$ mode than $A_{1\,g}$. This is because the G of $E_{2\,g}$ mode represents the energy coupling factor of combined LO and TO phonons. Therefore, this number should higher than that of $A_{1\,g}$, which is only for ZO phonons. Note that here the G value is calculated using the results of the 20 × objective because k and D have minimum effects on our calculation under this heating state compared with the two others. This was also shown in Fig. 3(a).

3. Discussion

Fig. 4(c) shows that the thermal non-equilibrium between phonon branches is significant, and it is stronger under smaller heating areas. Also, for all three samples, it is observed that this non-equilibrium is stronger between in-plane OP ($E_{2\,g}$ mode) and AP than the out-of-plane OP ($A_{1\,g}$ mode) and AP, while the ΔT^*_{OP} of both modes are almost identical (Fig. 4(b)). This is due to the weaker coupling between in-plane OP modes and all AP modes, namely higher ΔT_{OA} values, as shown in Fig. 4(c). Regarding the ΔT_{OA}% changes with film's thickness, a non-monotonic trend is observed (Fig. 4(c)). This could be caused by two reasons which play opposite roles. First, as it is mentioned in the next paragraph, an interfacial thermal non-equilibrium exists between phonon branches at the MoS_2-quartz boundary and can contribute to the total ΔT_{OA}%. This effect is more significant for the thinner films. Second, the laser absorption increases with the increased thickness; therefore, to get the same temperature rise for two different samples, a lower laser intensity is needed for thicker samples. This leads to lower ΔT_{OA}% for thicker samples.

Comparing the $R\prime\prime_{\mathrm{tc}}$ values in Tables 1 and 2, we see that $R\prime\prime_{\mathrm{tc}}$ is decreased after considering the thermal non-equilibrium effects, and FET-Raman could over predict $R\prime\prime_{\mathrm{tc}}$ up to ~25%. This number could be up to 100% for other optothermal thermal techniques based on Raman spectroscopy, such as steady-state Raman. For instance, for Sample #3 and under 100 × objective, the ΔT_{AP} to ΔT_{OP} ratio is around 50%. Therefore, neglecting the OP-AP non-equilibrium and equating ΔT_{AP} with ΔT_{OP} could result in a significant error. Also, it is observed that $R\prime\prime_{\mathrm{tc}}$ measured using the $A_{1\,g}$ mode is larger than the one measured by $E_{2\,g}$ mode. It is shown in the works by Ruan's group by non-equilibrium molecular dynamics simulations that different acoustic phonon branches have different interface resistance [39,41]. This will affect the temperature rise sensed by each of $E_{2\,g}$ and $A_{1\,g}$ modes and subsequently the measured $R\prime\prime_{\mathrm{tc}}$ using each of them. In fact, the optical-acoustic phonon temperature difference studied in this work consists of two parts as $\Delta T_{\mathrm{OA}} = \Delta T_{\mathrm{OA,I}} + \Delta T_{\mathrm{OA,R}}$, where $\Delta T_{\mathrm{OA,I}}$ is the optical-acoustic phonon temperature difference induced by photon energy absorption and the inter-phonon mode cascading energy transport, and is $\propto I$. This part is precisely determined and subtracted by the experimental characterization detailed in this work. $\Delta T_{\mathrm{OA,R}}$ is the optical-acoustic phonon temperature difference induced by the difference of interface thermal resistances among different phonon branches. This problem has been explored by molecular dynamics modeling by Ruan's group [39]. Fig. 4 (f) shows the temperature drop of different modes of phonons across a graphene-BN interface. It is observed that because of the ballistic and diffusive phonon transport and the different interface thermal resistance of phonon modes, a significant thermal non-equilibrium exists among phonon modes. Such non-equilibrium indeed exists over a quite long thickness (>20 nm). Compared with the lumped phonon temperature (MD), the ZO phonon (detected by $A_{1\,g}$ Raman peak) has the highest temperature difference $\Delta T_{\mathrm{OA,R}}$. On the other hand, LO/TO phonons' temperature is quite close to that of the lumped phonons. Although this simulation is for graphene on BN, the general conclusion should also hold true for other 2D materials on a substrate. Since $\Delta T_{\mathrm{OA,R}}$ was not extracted in our physics model, the temperature rise based on $\psi_{A_{1g}}(\Delta T_{\mathrm{OP}})$ even after subtracting $\Delta T_{\mathrm{OA,I}}$ is still higher than the real lumped phonon temperature. This will make the calculated interface resistance higher. On other hand, for the $E_{2\,g}$ mode, it represents the LO/TO phonons, whose temperature is very close to that of lumped phonon. So after subtracting the effect of $\Delta T_{\mathrm{OA,I}}$, ΔT_{AP} based on $\psi_{E_{2g}}$ closely represents the real temperature rise of acoustic phonons. The determined interface thermal resistance will be very close to the intrinsic value of lumped acoustic phonons, and is lower than that determined by the $A_{1\,g}$ mode data. Based on Fig. 4(f), it is found that at the interface, the ratio of average phonon temperature drop over that of ZO phonons $\Delta T_{\mathrm{avg}}/\Delta T_{\mathrm{ZO}}$ is around 0.60 and 0.75 for smooth and mixed interfaces. Based on the interface resistance data summarized in Table 2, this ratio is 0.60–0.81, quite close that for graphene on BN.

The coupling factors determined in this work are one order of magnitude larger than the previously measured ones by Wang et al. for a suspended MoS_2 nm-thick film [28]. The ΔT_{OA}% is larger for the supported 2D materials compared with suspended ones due to the fact that the supported sample could conduct the heat to the substrate through

the interface, and therefore, higher laser power is needed in order to reach the same ΔT_{AP} as the suspended material. This higher laser power leads to the larger ΔT_{OA}%. Regarding the G factor, the higher G values of supported compared with the suspended ones could be due to the higher phonon-phonon scattering inside the supported film. Also, since a higher laser intensity is used for the supported sample, more free electrons are generated, and this results in further scatterings inside the supported MoS_2. As mentioned in work by Lu et al. [27], G is related to C_p (phonon volumetric heat capacity) and τ_p (phonon relaxation time) as: $G = C_p/\tau_p$. The phonon relaxation time (τ_p) is decreased with the increased scatterings, and subsequently, G is increased. In addition, in the work by Wang et al., an analytical solution as a function of laser spot size was found between the OP temperature rise, measured by CW laser Raman, and calculated AP temperature rise. The uncertainty caused by this data fitting could be one of the reasons for this discrepancy. However, as shown in previous sections, the AP temperature rise calculation in this work is almost independent of any uncertainty caused by input thermal and optical properties, while in that previous work, they could affect the AP temperature rise calculation. Also, the measured laser power absorption and Raman signal intensity calculation did not include the forward and backward Raman scattering and was simply assumed as I_a. This could lead to a significant difference between the amount of absorbed laser power and calculated Raman intensity-weighted average temperature rise by a thin film (more than 50%). Another point worth mentioning here is that the G factor determined using $E_{2\,g}$ mode is larger than $A_{1\,g}$ ones. Therefore, the difference between G determined by using in-plane and out-of-plane modes could be attributed to C_p and τ_p. Also, the optical properties of MoS_2, i.e., refractive index and extinction coefficient, are a function of the incident laser wavelength. And this affects the laser absorption level of the thin film. Although it changes the absolute value of ΔT_{OP} and ΔT_{AP}, their relative value will be intact since our analysis is based on unit absorbed laser power. Therefore, ΔT_{OA}% and $R/\!/_{tc}$ will be untouched. However, as shown by Eq. (6) & (7), it will affect the G factor calculation, and this is considered in our analysis in detail.

4. Conclusion

In summary, we have developed a novel Raman optothermal technique coupled with a TMM Raman signal calculation to characterize the thermal non-equilibrium between optical and acoustic phonons under intense laser irradiation. Also, for the first time, the interfacial thermal transport between a nm-thick film and substrate is determined by considering this non-equilibrium effect. Furthermore, the energy coupling factor between OP and AP was determined for both in-plane and out-of-plane OP modes and is on order of $\sim 10^{15}$ $Wm^{-3}K^{-1}$. Our results indicate that the thermal non-equilibrium is significant, especially under smaller heating areas, and ignoring it as in previous classical optothermal works, could lead to considerable errors in determining thermal properties. In fact, neglecting these effects can over-predict $R/\!/_{tc}$ by up to 100%. Also, our results uncovered thermal non-equilibrium induced by ballistic and diffusive phonon transport and different interface thermal resistances of phonon modes. The ZO mode has a higher temperature than LO/TO mode due to such effect. In contrast to previous works, the numerical part of this work has a minimum dependency on the input values of thermal properties of materials, which makes our results more reliable. This technique could be used to characterize other 2D materials and study the thermal non-equilibrium between OP and AP inside them under laser irradiation. Also, it could be extended to other geometries, such as suspended thin-films.

5. Methods

5.1. Mechanical exfoliation and sample preparation

MoS_2 flakes are mechanically exfoliated from bulk crystal (429MS-AB, molybdenum disulfide, small crystals from the U.S.A., SPI Suppliers) using adhesive scotch tape. The peeled-off flakes are transferred to gel films (Gel-Film, PF-20/1.5-X4, Gel-Pak). Using two 3D nano stages, the gel film and quartz substrate are brought in contact, and the flake is transferred to the substrate by pressing it gently and moving it away from quartz. Subsequently, the morphology and size of the prepared MoS_2 films are characterized by optical and atomic force microscopes (NMAFM-2, Digital Instruments, CA, USA).

5.2. Raman spectroscopy measurement

The Raman measurement in this work is conducted with a Raman system in the backscattering configuration consisting of a 532 nm continuous wave laser (Excelsior-532-150-CDRH, Spectra-Physics), a Raman spectrometer (Voyage, B&W Tek, Inc.), and a microscope (Olympus BX53), as the main parts of the system. The laser power is adjusted using a neutral density (ND) filter that is controlled by a LabView program for precise measurement of the power dependence of each Raman mode's wavenumber shift (RSC values introduced in the physics section). For more about this Raman system, see our previous works [42–44].

5.3. 3D numerical model and governing equations for T_{AP} calculation

The theoretical calculation of the local lumped AP temperature rise was conducted using a 3D numerical modeling program based on the finite volume method. The actual sample size and thickness are used in this calculation. The following two equations are used to simulate hot carrier generations and diffusions, and heat diffusion in the sample:

$$\frac{\partial \Delta N}{\partial t} = D\nabla^2 \Delta N - \frac{\Delta N}{\tau_{e-h}} + \frac{\partial n_0}{\partial T}\frac{\Delta T}{\tau_{e-h}} + \Phi\alpha, \tag{5}$$

$$\rho c_p \frac{\partial \Delta T}{\partial t} = k\frac{1}{r}\frac{\partial}{\partial r}\left(r\frac{\partial \Delta T}{\partial r}\right) + k_{\perp}\frac{\partial^2 \Delta T}{\partial z^2} + \alpha I\left(\frac{h\nu - E_g}{h\nu}\right) + \frac{E_g \Delta N}{\tau_{e-h}}, \tag{6}$$

where ΔN (cm^{-3}), $\tau_{e\text{-}h}$ (s), n_0 (m^{-3}), Φ (number of photons per $m^3 s$), α (cm^{-1}), and ΔT (K) are carrier concentration, electron-hole recombination time, equilibrium free carrier density at temperature T, incident photon flux, the optical absorption coefficient of MoS_2 films, and temperature rise, respectively. Also, k ($Wm^{-1}K^{-1}$), $k_{\perp}$ ($Wm^{-1}K^{-1}$), $h\nu$ (2.33 eV for the 532 nm laser), and E_g are in-plane thermal conductivity of MoS_2, out-of-plane thermal conductivity of MoS_2, photon energy of the laser beam, and MoS_2 bandgap, respectively. Note that under the CW laser heating, the left-hand side terms of both equations (time-dependent terms) are zero. Here, $k_{\perp}$, ρc_p, and E_g of MoS_2 takes 5 $Wm^{-1}K^{-1}$, 1.89 $MJm^{-3}K^{-1}$, and 1.4 eV, respectively [45,46]. As reported in our previous works, their values have negligible effects on $\Theta_{F20,th}$ and Φ_{th} [16]. The laser heating source term (I) under both states (only during on-time for amplitude-modulated laser) in cylindrical coordinate is governed by:

$$I\left(r,z\right) = \frac{I_0}{\tau_L}\exp\left(-\frac{r^2}{r_0^2}\right)\exp\left(-\frac{z}{\tau_L}\right) \tag{7}$$

Here, I_0 ($W\,m^{-2}$) and τ_L (m) are laser intensity ($= P/\pi r_0^2$) and laser absorption depth, respectively. τ_L is determined as: $\lambda/4\pi k_L = 36.5$ nm, where k_L is the extinction coefficient and is ~1.16 under 532 nm laser (λ) for MoS_2 [47]. Here, 1 mW irradiating laser (P) is used to calculate the AP temperature rise. The amount of absorbed laser power (I_a) is calculated as: $I_a = P \times \{1 - [(n_{MoS_2} - 1)/(n_{MoS_2} + 1)]^2\} \times [1 - \exp(-t/\tau_L)]$. Here, n_{MoS_2} is the refractive index of MoS_2 under 532 nm laser and the second term of this equation shows the transmitted power based on the Fresnel reflectivity equation. Here, n_{MoS_2} is ~5.237 [47]. Using these three equations, the temperature rise (T) at each location (r, z) is calculated, and Raman-intensity weighted average temperature rises (ΔT_{CW20}, ΔT_{CW50}, ΔT_{CW100}, and ΔT_{F20}) are determined as: $\int_0^V Ie^{-z/\tau_L} Td\nu/$

$\int_0^V Ie^{-z/\tau_L}dv$ and. $\int_0^t \int_0^V Ie^{-z/\tau_L}Tdvdt/\int_0^t \int_0^V Ie^{-z/\tau_L}dvdt.$, for CW and amplitude-modulated CW lasers, respectively. Here, V is the volume of the sample, and the term e^{-z/τ_L} represents the Raman signal attenuation when the signal leaves the scattering location.

5.4. Physics of FET-Raman

As mentioned in Section 2.3, two different laser heating modes of steady-state and transient state are constructed to perform FET-Raman. Fig. 1(e) indicates the Raman shift (ω) and temperature evolution of MoS_2 film during the pulsed laser heating. During pulse on-time (t_h), the sample's temperature increases, which leads to the redshift of ω for both Raman modes. Here, heating and cooling times are equal: $t_h = t_c = 1/(2f)$. For the 500 kHz modulated laser that is used in this work, t_h and t_c are 1 μs. Under both states, we do not measure the absolute temperature rise of the MoS_2 like that in steady-state Raman optothermal techniques. Instead, the excited Raman signal is collected under various laser powers (P), and the Raman shift of both $E_{2\,g}$ and $A_{1\,g}$ are recorded under these powers. The measured RSC values (ψ_{CW20} and ψ_{F20}) could be written as: $\psi_{CW20} = \partial\omega/\partial P \propto \alpha(\partial\omega/\partial T)f_1(k, D, R_{int})$ and $\psi_{F20} = \partial\omega/\partial P \propto \alpha(\partial\omega/\partial T)f_2(k, D, R_{int}, \rho c_p)$. Here, α is the laser absorption coefficient of MoS_2 film. Then, the normalized RSC is determined as: $\Theta_{F20} = \psi_{F20}/\psi_{CW20} \propto f_2(k,D,R_{int},\rho c_p)/f_1(k,D,R_{int})$. This shows that there is no effect of α and $(\partial\omega/\partial T)$ in Θ_{F20}. Using our 3D numerical model, the local lumped Raman intensity-weighted average AP temperature rises under both states (ΔT_{CW20} and ΔT_{F20}) are calculated for several k, D, and R''_{tc} values using known ρc_p as mentioned in the previous paragraph, and $\Theta_{F20,th}$ is calculated as: $\Theta_{F20,th} = \Delta T_{F20}/\Delta T_{CW20}$. $\Theta_{F20,th}$ does not depend on k, D, and ρc_p, and is only function of R''_{tc}. The different contributions of R''_{tc} to ΔT_{CW20} and ΔT_{F20} could be illustrated by estimating the total thermal resistance between MoS_2 and quartz, which is the sum of the interfacial thermal resistance (R_T) and thermal resistance of quartz (R_{sub}). For both heating states, R_T is $R''_{tc}/\pi r_0^2$. However, under CW and amplitude-modulated laser heating, R_{sub} is $1/4r_0k_{sub}$ and $2\sqrt{\alpha_{sub}t_0}/\pi r_0^2 k_{sub}$, respectively. This shows the different contributions of R''_{tc} to the total thermal resistance ($R_T + R_{sub}$). This is shown in Fig. 1(f) and our previous works about FET-Raman [12,48]. Therefore, we are able to find R''_{tc} by calculating $\Theta_{F20,th}$ for a range of R''_{tc}, and equating it with the experimental Θ_{F20}.

Under pulsed laser heating, two extreme scenarios could be observed. If f is very low, the sample's temperature rise will reach the steady-state during the heating period (t_h) and will cool down totally during the laser-off time or cooling period (t_c). These two periods are shown in Fig. 1(e). Under this situation, the average temperature rise is $T_{f,low}$ and is similar to a steady heating state without any frequency modulation. If f takes a very high value, t_h and t_c will be very short, and the temperature variation during them will be very small. This state is called a quasi-steady state, and the average temperature rise is $T_{f,high}$. It is proved in our previous works that $T_{f,high}/T_{f,low} \simeq 0.5$ [49,50], and the sensitivity of FET-Raman is maximum when f is picked in a way that $T_f/T_{f,low} = T_f/T_{ss} \simeq 0.75$. Here, T_f and T_{sss} are the average local AP temperature rise under transient (amplitude modulation) and steady (CW laser) states, respectively. Fig. S2 shows our numerical analysis for a MoS_2 film to find the appropriate f. T_f/T_{ss} is calculated for a reasonable range of R''_{tc} and is shown that the sensitivity of FET-Raman to R''_{tc} is maximum when f is between 400 and 600 kHz.

CRediT authorship contribution statement

H. Zobeiri, **C. Deng**, **Q. Zhang** and **X. Wang** conceived the experimental design and physics idea. **H. Zobeiri** and **N. Hunter** conducted experiments and data processing. **N. V. Velson** developed the optics physics model and computation program. All authors conducted results analysis and data physical interpretation. All authors participated in manuscript preparation.

Declaration of Competing Interest

The authors declare that they have no known competing financial interests or personal relationships that could have appeared to influence the work reported in this paper.

Acknowledgement

Partial support of this work by National Science Foundation (CBET1930866 and CMMI2032464) and the Science and Technology Research Program of Chongqing Municipal Education Commission (Grant No. KJQN201901528) is gratefully acknowledged. C.D. is supported by the Guangdong Basic and Applied Basic Research Foundation (No. 2020A1515110699).

Appendix A. Supporting information

Supplementary data associated with this article can be found in the online version at doi:10.1016/j.nanoen.2021.106364.

References

[1] H. Malekpour, A.A. Balandin, Raman-based technique for measuring thermal conductivity of graphene and related materials, J. Raman Spectrosc. 49 (1) (2018) 106–120.
[2] S. Sahoo, A.P.S. Gaur, M. Ahmadi, M.J.F. Guinel, R.S. Katiyar, Temperature-dependent Raman studies and thermal conductivity of few-layer MoS_2, J. Phys. Chem. C 117 (17) (2013) 9042–9047.
[3] X. Zhang, D. Sun, Y. Li, G.-H. Lee, X. Cui, D. Chenet, Y. You, T.F. Heinz, J.C. Hone, Measurement of lateral and interfacial thermal conductivity of single-and bilayer MoS_2 and $MoSe_2$ using refined optothermal Raman technique, ACS Appl. Mater. Interfaces 7 (46) (2015) 25923–25929.
[4] R. Wang, T. Wang, H. Zobeiri, P. Yuan, C. Deng, Y. Yue, S. Xu, X. Wang, Measurement of the thermal conductivities of suspended MoS_2 and $MoSe_2$ by nanosecond ET-Raman without temperature calibration and laser absorption evaluation, Nanoscale 10 (48) (2018) 23087–23102.
[5] P. Yuan, R. Wang, T. Wang, X. Wang, Y. Xie, Nonmonotonic thickness-dependence of in-plane thermal conductivity of few-layered MoS_2: 2.4 to 37.8 nm, Phys. Chem. Chem. Phys. 20 (40) (2018) 25752–25761.
[6] S. Xu, A. Fan, H. Wang, X. Zhang, X. Wang, Raman-based nanoscale thermal transport characterization: a critical review, Int. J. Heat. Mass Transf. 154 (2020), 119751.
[7] H. Lin, R. Wang, H. Zobeiri, T. Wang, S. Xu, X. Wang, In-Plane Structure Domain Size of nm-thick $MoSe_2$ Uncovered by Low-momentum Phonon Scattering, Nanoscale (2021).
[8] J. Gao, H. Zobeiri, H. Lin, D. Xie, Y. Yue, X. Wang, Coherency between thermal and electrical transport of partly reduced graphene paper, Carbon 178 (2021) 92–102.
[9] Y. Xie, M. Han, R. Wang, H. Zobeiri, X. Deng, P. Zhang, X. Wang, Graphene aerogel based bolometer for ultrasensitive sensing from ultraviolet to far-infrared, ACS Nano 13 (5) (2019) 5385–5396.
[10] R. Wang, T. Wang, H. Zobeiri, D. Li, X. Wang, Energy and charge transport in 2D atomic layer materials: Raman-based characterization, Nanomaterials 10 (9) (2020) 1807.
[11] M.R. Hajidavalloo, F. Ayatolah Zadeh Shirazi, M. Mahjoob, Energy cost minimization in an electric vehicle solar charging station via dynamic programming, J. Comput. Appl. Mech. 51 (2) (2020) 275–280.
[12] N. Hunter, N. Azam, H. Zobeiri, R. Wang, M. Mahjouri-Samani, X. Wang, Interfacial thermal conductance between monolayer WSe_2 and SiO_2 under consideration of radiative electron–hole recombination, ACS Appl. Mater. Interfaces 12 (45) (2020) 51069–51081.
[13] P. Yuan, R. Wang, H. Tan, T. Wang, X. Wang, Energy transport state resolved raman for probing interface energy transport and hot carrier diffusion in few-layered MoS_2, ACS Photonics 4 (12) (2017) 3115–3129.
[14] H. Zobeiri, N. Hunter, R. Wang, X. Liu, H. Tan, S. Xu, X. Wang, Thermal conductance between water and nm-thick WS_2: extremely localized probing using nanosecond energy transport state-resolved Raman, Nanoscale Adv. 2 (12) (2020) 5821–5832.
[15] M. Bergler, K. Cvecek, F. Werr, M. Brehl, D. De Ligny, M. Schmidt, Cooling rate calibration and mapping of ultra-short pulsed laser modifications in fused silica by Raman and Brillouin spectroscopy, Int. J. Extrem. Manuf. 2 (3) (2020), 035001.
[16] H. Zobeiri, R. Wang, Q. Zhang, G. Zhu, X. Wang, Hot carrier transfer and phonon transport in suspended nm WS_2 films, Acta Mater. 175 (2019) 222–237.
[17] P. Yuan, J. Liu, R. Wang, X. Wang, The hot carrier diffusion coefficient of sub-10 nm virgin MoS_2: uncovered by non-contact optical probing, Nanoscale 9 (20) (2017) 6808–6820.
[18] R. Wang, S. Xu, Y. Yue, X. Wang, Thermal behavior of materials in laser-assisted extreme manufacturing: Raman-based novel characterization, Int. J. Extrem. Manuf. 2 (3) (2020), 032004.

[19] Z. Ahmadi, B. Yakupoglu, N. Azam, S. Elafandi, M. Mahjouri-Samani, Self-limiting laser crystallization and direct writing of 2D materials, Int. J. Extrem. Manuf. 1 (1) (2019), 015001.

[20] M.R. Hajidavalloo, F.A. Shirazi, M.J. Mahjoob, Performance of different optimal charging schemes in a solar charging station using dynamic programming, Optim. Control Appl. Methods 41 (5) (2020) 1568–1583.

[21] K.F. Mak, J. Shan, Photonics and optoelectronics of 2D semiconductor transition metal dichalcogenides, Nat. Photonics 10 (4) (2016) 216–226.

[22] A.K. Vallabhaneni, D. Singh, H. Bao, J. Murthy, X. Ruan, Reliability of Raman measurements of thermal conductivity of single-layer graphene due to selective electron-phonon coupling: a first-principles study, Phys. Rev. B 93 (12) (2016), 125432.

[23] H. Zobeiri, N. Hunter, R. Wang, T. Wang, X. Wang, Direct characterization of thermal nonequilibrium between optical and acoustic phonons in graphene paper under photon excitation, Adv. Sci. (Weinh. Baden. Wurtt. Ger.) 8 (2021), 2004712.

[24] S. Sullivan, A. Vallabhaneni, I. Kholmanov, X. Ruan, J. Murthy, L. Shi, Optical generation and detection of local nonequilibrium phonons in suspended graphene, Nano Lett. 17 (3) (2017) 2049–2056.

[25] D.A. Broido, M. Malorny, G. Birner, N. Mingo, D.A. Stewart, Intrinsic lattice thermal conductivity of semiconductors from first principles, Appl. Phys. Lett. 91 (23) (2007), 231922.

[26] Z. Tian, K. Esfarjani, J. Shiomi, A.S. Henry, G. Chen, On the importance of optical phonons to thermal conductivity in nanostructures, Appl. Phys. Lett. 99 (5) (2011), 053122.

[27] Z. Lu, A. Vallabhaneni, B. Cao, X. Ruan, Phonon branch-resolved electron-phonon coupling and the multitemperature model, Phys. Rev. B 98 (13) (2018), 134309.

[28] R. Wang, H. Zobeiri, Y. Xie, X. Wang, X. Zhang, Y. Yue, Distinguishing optical and acoustic phonon temperatures and their energy coupling factor under photon excitation in nm 2D materials, Adv. Sci. (Weinh. Baden. Wurtt. Ger.) 7 (2020), 2000097.

[29] M. Hong, K. Zheng, W. Lyv, M. Li, X. Qu, Q. Sun, S. Xu, J. Zou, Z.-G. Chen, Computer-aided design of high-efficiency GeTe-based thermoelectric devices, Energy Environ. Sci. 13 (6) (2020) 1856–1864.

[30] M. Hong, Y. Wang, T. Feng, Q. Sun, S. Xu, S. Matsumura, S.T. Pantelides, J. Zou, Z.-G. Chen, Strong phonon–phonon interactions securing extraordinary thermoelectric $Ge_{1-x}Sb_xTe$ with Zn-alloying-induced band alignment, J. Am. Chem. Soc. 141 (4) (2018) 1742–1748.

[31] H. Zobeiri, R.D. Wang, T.Y. Wang, H. Lin, C. Deng, X.W. Wang, Frequency-domain energy transport state-resolved Raman for measuring the thermal conductivity of suspended nm-thick $MoSe_2$, Int. J. Heat. Mass Transf. 133 (2019) 1074–1085.

[32] J.L. Verble, T.J. Wieting, Lattice mode degeneracy in MoS_2 and other layer compounds, Phys. Rev. Lett. 25 (6) (1970) 362–365.

[33] C. Sourisseau, F. Cruege, M. Fouassier, M. Alba, Second-order Raman effects, inelastic neutron scattering and lattice dynamics in 2H-WS_2, Chem. Phys. 150 (2) (1991) 281–293.

[34] I. Chatzakis, H. Yan, D. Song, S. Berciaud, T.F. Heinz, Temperature dependence of the anharmonic decay of optical phonons in carbon nanotubes and graphite, Phys. Rev. B 83 (20) (2011), 205411.

[35] P.G. Klemens, Anharmonic decay of optical phonons, Phys. Rev. 148 (2) (1966) 845–848.

[36] R.A. Escobar, C.H. Amon, Influence of phonon dispersion on transient thermal response of silicon-on-insulator transistors under self-heating conditions, (2007).

[37] L. Chen, S. Kumar, Thermal transport in graphene supported on copper, J. Appl. Phys. 112 (4) (2012), 043502.

[38] X. Gu, B. Li, R. Yang, Layer thickness-dependent phonon properties and thermal conductivity of MoS2, J. Appl. Phys. 119 (8) (2016), 085106.

[39] T. Feng, W. Yao, Z. Wang, J. Shi, C. Li, B. Cao, X. Ruan, Spectral analysis of nonequilibrium molecular dynamics: spectral phonon temperature and local nonequilibrium in thin films and across interfaces, Phys. Rev. B 95 (19) (2017), 195202.

[40] N.V. Velson, H. Zobeiri, X. Wang, Rigorous prediction of Raman intensity from multi-layer films, Opt. Express 28 (23) (2020) 35272–35283.

[41] T. Feng, Y. Zhong, J. Shi, X. Ruan, Unexpected high inelastic phonon transport across solid-solid interface: Modal nonequilibrium molecular dynamics simulations and Landauer analysis, Phys. Rev. B 99 (4) (2019), 045301.

[42] H. Zobeiri, R. Wang, C. Deng, Q. Zhang, X. Wang, Polarized Raman of nanoscale two-dimensional materials: combined optical and structural effects, J. Phys. Chem. C 123 (37) (2019) 23236–23245.

[43] H. Zobeiri, S. Xu, Y.A. Yue, Q.Y. Zhang, Y.S. Xie, X.W. Wang, Effect of temperature on Raman intensity of nm-thick WS_2: combined effects of resonance Raman, optical properties, and interface optical interference, Nanoscale 12 (10) (2020) 6064–6078.

[44] S. Xu, H. Zobeiri, N. Hunter, H. Zhang, G. Eres, X. Wang, Photocurrent in carbon nanotube bundle: graded seebeck coefficient phenomenon, Nano Energy 86 (2021), 106054.

[45] J. Liu, G.-M. Choi, D.G. Cahill, Measurement of the anisotropic thermal conductivity of molybdenum disulfide by the time-resolved magneto-optic Kerr effect, J. Appl. Phys. 116 (23) (2014), 233107.

[46] C. Yim, M. O'Brien, N. McEvoy, S. Winters, I. Mirza, J.G. Lunney, G.S. Duesberg, Investigation of the optical properties of MoS_2 thin films using spectroscopic ellipsometry, Appl. Phys. Lett. 104 (10) (2014), 103114.

[47] A.R. Beal, H.P. Hughes, Kramers-Kronig analysis of the reflectivity spectra of 2H–MoS_2, 2H–$MoSe_2$ and 2H–$MoTe_2$, J. Phys. C Solid State Phys. 12 (5) (1979) 881–890.

[48] T.L. Bergman, A. Lavine, F.P. Incropera, D.P. Dewitt, Fundamentals of Heat and Mass Transfer, John Wiley & Sons New York, 2017.

[49] R. Wang, H. Zobeiri, H. Lin, W. Qu, X. Bai, C. Deng, X. Wang, Anisotropic thermal conductivities and structure in lignin-based microscale carbon fibers, Carbon 147 (2019) 58–69.

[50] T. Wang, S. Xu, D.H. Hurley, Y. Yue, X. Wang, Frequency-resolved Raman for transient thermal probing and thermal diffusivity measurement, Opt. Lett. 41 (1) (2016) 80–83.